Research article

Adi Salomon, Heiko Kollmann, Manfred Mascheck, Slawa Schmidt, Yehiam Prior, Christoph Lienau and Martin Silies*

Space- and time-resolved second harmonic spectroscopy of coupled plasmonic nanocavities

https://doi.org/10.1515/nanoph-2021-0049
Received February 4, 2021; accepted April 19, 2021;
published online May 12, 2021

Abstract: Localized surface plasmon resonances of individual sub-wavelength cavities milled in metallic films can couple to each other to form a collective behavior. This coupling leads to a delocalization of the plasmon field at the film surface and drastically alters both the linear and nonlinear optical properties of the sample. In periodic arrays of nanocavities, the coupling results in the formation of propagating surface plasmon polaritons (SPP), eigenmodes extending across the array. When artificially introducing dislocations, defects and imperfections, multiple scattering of these SPP modes can lead to *hot-spot* formation, intense and spatially confined fluctuations of the local plasmonic field within the array. Here, we study the underlying coupling effects by probing plasmonic modes in well-defined individual triangular dimer cavities and in arrays of triangular cavities with and without artificial defects. Nonlinear confocal spectro-microscopy is employed to map the second harmonic (SH) radiation from these systems. Pronounced spatial localization of the SPP field and significant enhancements of the SH intensity in certain, randomly distributed hot spots by more than an order of magnitude are observed from the triangular arrays as compared to a bare silver film by introducing a finite degree of disorder into the array structure. Hot-spot formation and the resulting enhancement of the nonlinear efficiency are correlated with an increase in the lifetime of the localized SPP modes. By using interferometric SH autocorrelation measurements, we reveal lifetimes of hot-spot resonances in disordered arrays that are much longer than the few-femtosecond lifetimes of the localized surface plasmon resonances of individual nanocavity dimers. This suggests that hot spot lifetime engineering provides a path for manipulating the linear and nonlinear optical properties of nanosystems by jointly exploiting coherent couplings and tailored disorder.

Keywords: Babinet's principle; enhanced lifetime; localization; surface plasmon polaritons.

1 Introduction

The interaction of light with individual metallic nanostructures leads to the excitation of localized surface plasmon (LSPs) modes, i.e., resonant and collective oscillations of the conduction electrons in the metal nanoparticle which are coupled to the surrounding electromagnetic field. Their resonance frequencies are determined by the geometrical parameters of the metallic nanostructure and the polarizability of both the metal and the surrounding medium. These collective charge oscillations cause a large resonant enhancement of the local field near the particle and this field enhancement is proportional to the damping time of the LSP resonance [1, 2]. Damping of surface plasmons occurs by emitting radiation or by transforming radiation into heat [3].

Nanoparticles and nanovoids (cavities) in far-field optics are complementary to each other according to Babinets principle, yet, their hybridization/coupling is found to be different [4]. While adjacent nanoparticles are coupled via their electromagnetic near- and/or far-fields [5], the coupling between adjacent nanocavities generally relies on the exchange of propagating surface plasmon polaritons (SPPs), surface-bound waves at the metal-dielectric

*Corresponding author: Martin Silies, Institute of Physics and Center for Molecular and Nanoscale Science, Carl von Ossietzky Universität Oldenburg, D-26129 Oldenburg, Germany,
E-mail: martin.silies@uol.de. https://orcid.org/0000-0002-3704-2066
Adi Salomon, Department of Chemistry, Bar-Ilan University, BINA nano-center, Ramat-Gan, 52900, Israel; and Department of Chemical and Biological Physics, Weizmann Institute of Science, 76100 Rehovot, Israel
Heiko Kollmann, Manfred Mascheck, Slawa Schmidt and Christoph Lienau, Institute of Physics and Center for Molecular and Nanoscale Science, Carl von Ossietzky Universität Oldenburg, D-26129 Oldenburg, Germany. https://orcid.org/0000-0003-3854-5025 (C. Lienau)
Yehiam Prior, Department of Chemical and Biological Physics, Weizmann Institute of Science, 76100 Rehovot, Israel

interface of the thin metal film that is supporting the cavities [6]. In larger arrays of nanocavities, the interference of SPPs that are multiply scattered at the cavities often leads to localized regions of high SPP field amplitude ("hot-spots") in the plane of the metal film [7–12]. This SPP localization largely alters the linear and in particular also the nonlinear optical properties, e.g., the generation of second harmonic (SH) [4, 13], surface enhanced Raman scattering [14], or photoelectron [15–17] signals from the film. The nonlinear properties such as SH generation from metallic nanostructures are well documented and are attributed mainly to the enhanced EM field due to plasmonic excitations [7, 9, 18–20]. However, less reports exist on the coupling between plasmonic modes which give rise to enhanced SH generation and in particular to the lifetimes of coupled SPP modes. So far, very little is, in fact, known about the interplay between SPP localization and lifetime in coupled nanocavity systems.

Here, we combine confocal SH microscopy and interferometric frequency-resolved autocorrelation measurements with few-cycle time resolution to directly study the correlation between SH responses and lifetimes of localized SPP modes in coupled nanocavity systems. We use these techniques to study three model structures, all composed of the same sub-unit, an equilateral triangle. These are: (i) dimers of two triangular cavities, (ii) an ordered periodic array of triangular cavities, and (iii) a similar array with a periodicity that is broken by stitching errors induced during fabrication. We show that both SH yield and lifetime are greatly affected by the artificially introduced disorder in the array. We observe SH yields that are up to five times higher than those of the dimer array and SPP field decay times increasing from 2 fs in the dimer array to up to 13 fs in the disordered array. The demonstrated correlation between SPP lifetime and SH yield introduces an interesting new control parameter for tailoring the nonlinear optical properties of the disordered plasmonic systems.

2 Materials and methods

2.1 Nonlinear, time-resolved spectro-microscopy

The experimental set-up for the optical characterization is shown schematically in Figure 1(a) and in more detail in Fig. S1 of the Supplementary material. The nanostructured silver films are illuminated by dispersion-compensated 6-fs laser pulses derived from a commercial Ti:Sapphire oscillator (Femtolasers Rainbow) operating at a repetition rate of 82 MHz with a spectrum ranging from 650 to 1030 nm. A home-built dispersion-balanced Mach–Zehnder interferometer is implemented to generate a collinearly propagating pair of pulses with an electric field $E_L(t) + E_L(t+\tau)$ with variable time delay $\boldsymbol{\tau}$. By using an all-reflective Cassegrain objective (ARO) with a numerical aperture NA = 0.5 (Davin Optronics, 5004-000) the pulses are focused onto the sample at 0° incidence angle onto the silver film without losing the femtosecond temporal resolution [21]. Careful control of the spatial and temporal beam profile in the focus is essential in the reported experiments since the Cassegrain objective needs precise mechanical alignment to ensure sufficient beam quality. For this, we routinely characterize the beam profile laser light using light-scattering of subwavelength nanostructures [21]. In this reference, typical results

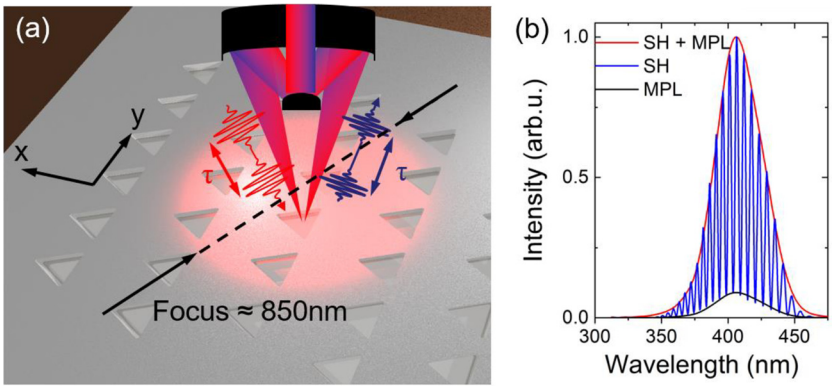

Figure 1: (a) Sketch of the confocal second harmonic (SH) microscopy technique. A dispersion-balanced pair of 6-fs-laser pulses with adjustable time delay $\boldsymbol{\tau}$ derived from a Ti:Sapphire oscillator and a Mach–Zehnder interferometer is focused by an all-reflective Cassegrain focusing objective onto the silver films containing the triangular nanocavities. The generated multiphoton photoluminescence (MPL) and SH from the samples is collected in reflection geometry by the same objective as a function of sample position and time delay $\boldsymbol{\tau}$ and analyzed in a spectrometer. (b) A prototypical spectrum taken at a position inside the triangular hole pattern. The signal consists of coherent SH and incoherent MPL emission. The blue line represents the measured spectrum showing the modulated SH emission between the red and black line and the black line represents the weak, spectrally unmodulated MPL.

demonstrating an essentially diffraction-limited beam profile with characteristic Airy rings resulting from the finite beam obscuration of the Cassegrain objective are presented. The pulse energy was kept at 50 pJ resulting in a peak intensity of $1.5 \cdot 10^{12}$ W/cm^2, well below the damage threshold of the structures but sufficiently high to cause efficient SH emission. The limited k-spectrum of the ARO, ranging from $k_{min} = \text{asin}(0.41 \cdot \text{NA}) = 11.8°$ to $k_{max} = \text{asin}(\text{NA}) = 30°$, results in a central spot with a diameter of 850 nm (full width at half maximum [FWHM]) and an Airy ring pattern that carries a maximum intensity of 6% of the central spot [21]. The focus diameter is larger than the average distance between two triangular holes. The polarization of the incident light is chosen to be parallel along the y-axis, i.e., along the long axis of dimer pattern and perpendicular to the baseline of the hexagonal pattern.

The nonlinear emission from the sample is detected between 350 and 480 nm in reflection geometry and analyzed in a spectrometer (SpectraPro-2500i, Acton) attached to a LN_2-cooled CCD camera (Spec-10, Princeton Instruments) while simultaneously raster-scanning the samples through the laser focus along the x- and y-direction using a 2D piezo scanner with a step size of 250 nm. Since the nonlinear emission at the SH rather than the linearly scattered light is detected, the spatial limit of the confocal microscope is improved to approximately 610 nm. By varying the time delay between the two pulses in the Mach–Zehnder interferometer with a step size of 200 as between −66 and +66 fs and by simultaneously detecting the light at the SH, interferometric frequency-resolved autocorrelation (IFRAC) traces at distinct positions on the samples are obtained. These IFRAC traces plot the measured nonlinear emission spectrum as a function of the time delay τ and can be used to directly extract the temporal structure of the local electric field $E_L(t)$ at the fundamental of the laser [22–24].

A characteristic nonlinear emission spectrum induced by such a pulse pair at a randomly chosen position on the triangular hole pattern is shown as a blue line in Figure 1(b) at a time delay of τ = 100 fs. By using a time-delayed pulse pair, an easy and fast separation between coherent SH and incoherent MPL is accomplished [25]: The spectrum consists of a time delay-dependent component $I_{SH}(\lambda)$ (area between red and black line) centered around 410 nm that oscillates at $\Delta\omega = 2\pi/\tau$ and a delay-independent, non-oscillating component $I_{MPL}(\lambda)$ centered around 405 nm (black line). While the oscillating component can be attributed to a coherent SH process, the delay-independent component is originating from an incoherent, multi-photon induced photoluminescence process [25]. In the experiment, we separated both components using a fast Fourier transformation filtering procedure.

2.2 Sample preparation

Silver films with a thickness of 200 nm were evaporated onto a clean fused silica glass under high vacuum. Atomic force microscope measurements of a bare silver film from a sample using the same production process revealed a surface roughness of less than 3 nm (peak-to-peak) [17]. A focused Gallium ion beam source (FEI Helios Nanolab 600i) was used to mill arrays of equilateral-shaped triangular nanocavities in the silver film. In the inset of Figure 2(a), a magnified view of a single triangular nanocavity is displayed. The side length of the triangles of a = 180 nm was chosen such that the main resonance – the whispering gallery mode (WGM) of the nanotriangle – is off-resonance to the exciting laser spectrum [4]. In Chapter S2 of the Supplementary material, a numerical analysis of the main resonance is presented that shows the main WGM resonance of the nanocavity for different side lengths of the equilateral triangle. For a side length of a = 180 nm, the WGM resonance is found at 1.70 eV and lies well outside the laser spectrum.

In the experiments, we investigate the nonlinear responses of thin silver films perforated with three different types of arrangement of these triangular cavities: (i) nanocavity dimers, (ii) a periodic, hexagonal array of nanotriangles, and (iii) a similar nanoparticle array with intentionally introduced defects and stitching errors (Figure 2a–c). All are composed of the same nanotriangular sub-unit. The dimers consist of pairs of vertically shifted triangle cavities, with the distance d_1 between the pairs being changed from 450 (left) to 300 nm (right) in steps of nominally 37.5 nm. Adjacent dimer cavities can be considered as noninteracting since the distance between them is about 2 µm along the y-axis and about 1.5 µm along the x-axis [26, 27]. In case of a finite coupling, we would expect signatures of SPP pulses that are multiply reflected between the triangles in the SH response of a nanocavity dimer in Figure 5(b) and (e) at time delays of $2s_{x,y}/c_p$ of 11 and 15 fs, respectively. Here, $s_{x,y}$ is the distance between the dimer cavities,

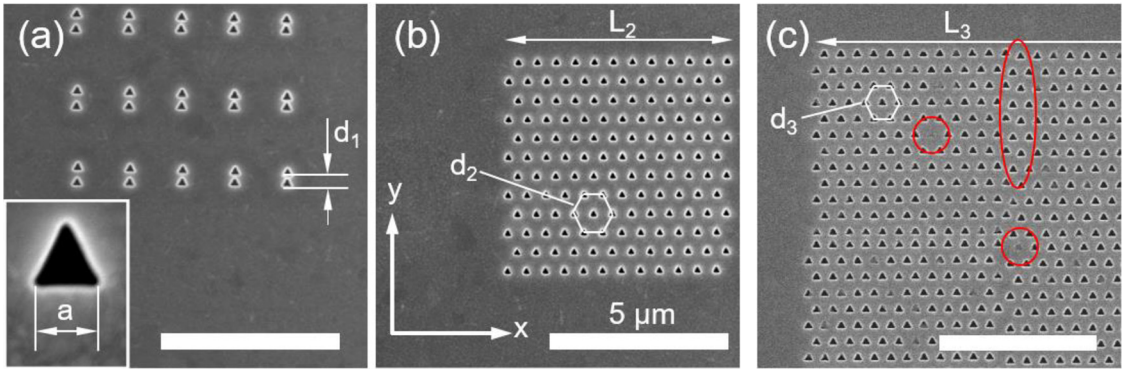

Figure 2: (a–c) Scanning electron micrographs of different triangular hole patterns with a base length of a = 180 nm milled into a 200 nm thick Ag film: (a) Dimers with variable inter-triangle separation d_1, (b) a hexagonal nanohole array with a lattice constant of d_2 = 500 nm, and (c) a hexagonal nanohole array with the same average lattice constant $d_3 = d_2$ but with intentionally introduced lattice defects and stitching errors, indicated in red. The inset in (a) shows a magnified view of a single triangular nanocavity with a side length of a = 180 nm. The scale bar in each image is fixed to 5 µm.

$c_p \approx 0.9 \cdot c_0$ as the group velocity of the SPP wave [28], and c_0 the speed of light in vacuum.

In Chapter S2 of the Supplementary material, linear transmission spectra for dimer cavities with different inter-triangular distances are presented. They show that the inter-triangle coupling results in a splitting of the transmission into two peaks, one near the WGM resonance of an individual nanotriangle, and a second, collective resonance that is red-shifted from the WGM resonance by up to 130 meV. The calculations predict that the red-shifted resonance is most pronounced for an interparticle distance of approximately 350 nm. Both resonances are spectrally well-separated from the exciting laser spectrum, resulting in a predominantly off-resonant excitation of the plasmon resonances in the experiments. The second sample is a hexagonal array of triangular cavities with a lattice constant of $d_2 = 500$ nm (Figure 2b). Here, special care was put on the homogeneity resulting in a highly regular hexagonal pattern with total dimensions of $L_2 = 6.45\ \mu m \times 6.45\ \mu m$. The third sample, shown in Figure 2(c), has the same geometrical parameters as in (b), i.e., $d_3 = 500$ nm, but with artificial lattice defects and stitching errors, some of them indicated by the large red ellipse and circles. The dimensions of the array are twice as large as in Sample 2, i.e., $L_3 = 12.9\ \mu m \times 12.9\ \mu m$. Since the lattice constants, i.e., the inverse of the grating constants of these arrays are smaller than the center wavelength of the laser pulses, the coupling of the laser to SPP excitations of the array is weak for normal incidence illumination. Indeed, the simulated transmission spectrum shown in Fig. S2(c) of the Supplementary material mainly shows a resonance around 1.69 eV, higher in energy than the photon energy of the excitation laser. Hence, also the hexagonal arrays are basically off-resonantly excited in the IFRAC experiments. We shall note, that while the dimensions of each individual nanoresonator remains constant in the three samples, the size and the complexity of the arrays increases from (a) to (c). The idea of choosing these structures and arrangement is to study a coherent coupling between the cavities and to see the effect of defects on the coupling between the triangular nanocavities.

3 Results and discussions

The spectrally-integrated, coherent SH emission $I_{SH}(x,y) = \int S_{SH}(x,y,\lambda)d\lambda$ from the three samples is detected as a function of the position of the laser focus on the sample and is depicted in Figure 3(a)–(c). In order to ensure the comparability of the different samples, $I_{SH}(x,y)$ is normalized to the average SH intensity $\langle I_{SH}\rangle$ that is detected from the silver itself, indicated by the red-dashed box.

3.1 Dimer

In the dimer sample, SH emission from individual nanotriangle pairs is clearly spatially resolved (see Figure 3(a)). While recent investigations suggest, that the SH is generated in the middle of the dimers, the spatial resolution in the experiment is not sufficient to clarify this [13]. The intensity ratio $I_{SH}(x,y)/\langle I_{SH}\rangle$ in this map is quite low, only about a factor of two higher than from the silver film, and for some of the dimers the signal is similar to that emanating from the silver itself. Not all the dimers show the same SH enhancement, though they are composed from nominally the same sub-unit. The SH enhancement clearly varies when changing the distance d_1 between the triangles and reaches a maximum at an inter-triangle distance of 350 nm. This distance-dependent variation of the SH signal is the signature that the cavities are indeed coupled to each other and that the coupling strength is dependent on the distance between them [26]. This is supported by the finite difference time domain (FDTD) simulations shown in S2 of the Supplementary material, which show a maximum red shift of the plasmon resonance, and thus an optimum overlap with the spectrum of the excitation laser, for an inter-triangle distance of 350 nm. In Chapter S3 of the Supplementary material, a more detailed investigation of SH from the dimers is shown which highlights this resonance behavior. Furthermore, we note that the polarization of the incoming field is along the interaction axis (Y-axis) of the dimer. At orthogonal polarization, the emanating SH responses from the structures were barely distinguishable (not shown). As can be seen in (b), the SH spectrum from a prototypical dimer (black line) is only slightly red-shifted to 406 nm compared to the silver background, centered at 403 nm (green line). The frequency-doubled spectrum of the exciting laser is shown in comparison as a grey-shaded background.

3.2 Hole array

The map of the SH intensity ratio for the triangular hole array is shown in Figure 3(c). An intense and spatially only slightly nonhomogeneous SH response from the array is observed, with very low intensity ratios of about two to three measured at the boundaries and higher ones of about six in the middle of the array. Some fluctuations of the SH intensity across the array are seen. We shall note that while the array contains the same triangular nanocavities as Sample 1, the average signal intensity is much higher compared to the dimer sample, even at the edge of the array which shows the weakest SH emission. The enhanced SH response is related to the coupling between several cavities which tends to delocalize the SPP resonance of the array across several nanocavities.

In addition to this spatial delocalization of the nonlinear response, some hot spots show a locally-enhanced value of $I_{SH}/\langle I_{SH}\rangle$. For the most intense hot spot, marked by a black- and red-dotted cross, this intensity ratio reaches 6.5, more than twice as strong as the most intense SH response of a single dimer structure.

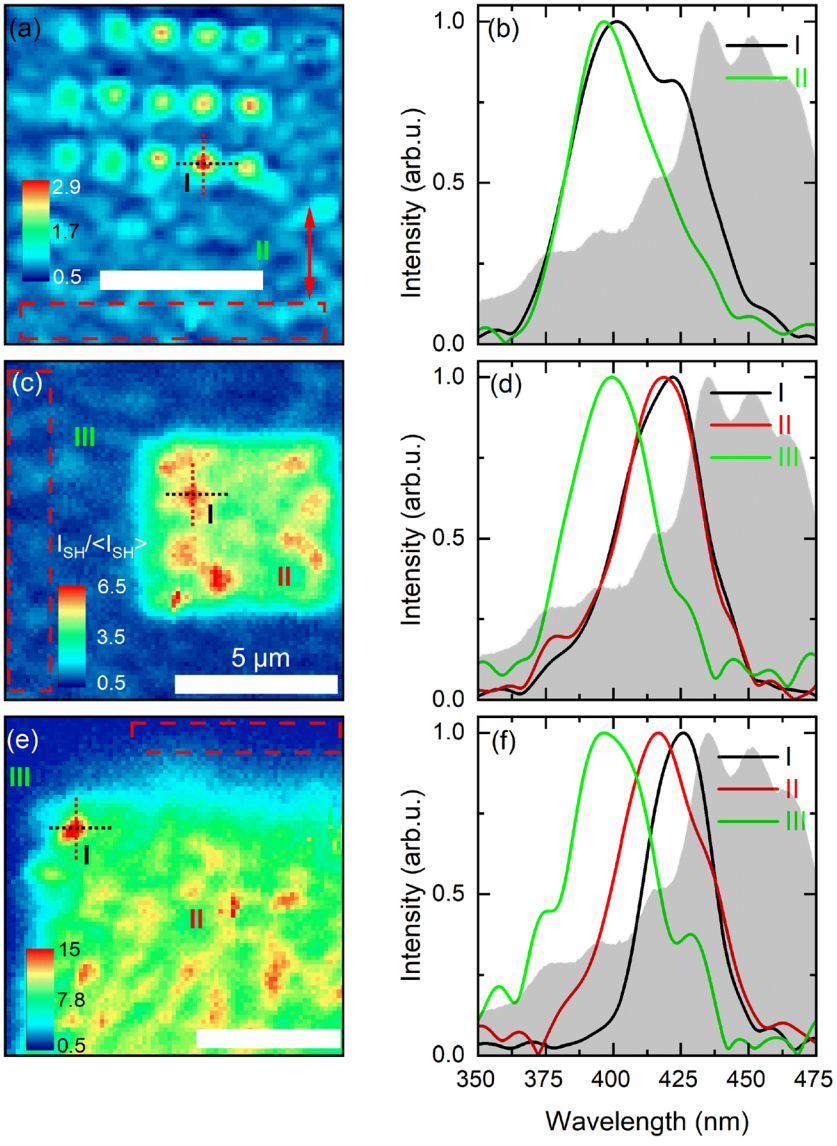

Figure 3: Second harmonic (SH) generation intensity maps (a, c, d) and prototypical spectra (b, d, f) of the three investigated structures: (a–b) a dimer of triangular holes, (c–d) a hexagonal hole array, and (e–f) a hexagonal hole array with defects. Left: in each image, the SH emission intensities are normalized to the average SH from the neighboring silver film, taken from the area marked by the red-dashed box. The black- and red-dotted cross indicates the most intense hot spot in each structure. The polarization of the incident light is along the *y*-axis for all measurements as indicated by the red arrow in (a). The scale bar of all images is 5 µm. All experiments are performed by exciting with 6-fs laser pulses centered at 880 nm. Right: normalized SH spectra from exemplary positions inside and outside the nanostructured arrays. The grey background shows the frequency-doubled spectrum of the Ti:Sapphire oscillator.

Typical spectra from the hexagonal array are depicted in (d). Again, the SH emitted from an arbitrary position within the array (red line) is red-shifted to 412 nm compared to the silver film (green line) at 401 nm, while the most intense hot spot is even red-shifted to 415 nm.

3.3 Stitched array

The map of $I_{SH}(x,y)/\langle I_{SH}\rangle$ for the stitched arrays is shown in Figure 3(e). The ratio between the local SH intensity and the average SH intensity reaches a value of 17.5, almost three times higher than the maximum in the array without defects in Figure 3(c). This value is also about a factor of two larger than the spatially-averaged SH signal inside the stitched array. These random fluctuations of the local SH response show that hot-spot formation and, thus, local variations of the surface plasmon field amplitude $E_{SP}(r)$ at the film surface, is more pronounced than in the ordered array. To quantify the local variations of $E_{SP}(r)$, we introduce a phenomenological local enhancement factor $f(r)$ by referencing this local field to the average field amplitude on the silver film $\langle E_{Ag}\rangle$. Since the local SH intensity is proportional to the fourth power of the local electric field, an average local field enhancement factor for the most dominant hot spot is estimated as:

$$f(\mathbf{r}) = E_{SP}(\mathbf{r})/\langle E_{Ag}(\mathbf{r})\rangle = \sqrt[4]{I_{SH}(\mathbf{r})/\langle I_{SH}\rangle} = 2.04 \qquad (1)$$

This field enhancement is about a factor of two lower than previously reported in similar systems [26]. For the stitched array, the observed redshift is most pronounced (see Figure 3(f)). The SH spectrum of a prototypical position

inside this array is centered around 415 nm (red line), compared to 401 nm for the silver film (green line). Finally, the center wavelength of the SH of the most pronounced hot spot within the stitched array is centered at 425 nm (black line), more than 20 nm red-shifted compared to the bare silver film.

Altogether, the red-shifted SH central wavelength for the hexagonal and especially the stitched hexagonal array is a strong indicator that the origin of the SH within the hexagonal array is a far-field dark mode [29] centered around a fundamental wavelength of 840–850 nm rather than the fundamental, far-field bright resonance of 750 nm (1.65 eV) of the hexagonal array, shown in Fig. S2(c) of the Supplementary material. In S4 of the Supplementary material, two-dimensional maps of both the center wavelength and of the spectral width are shown that show the observed redshift in more detail.

Beside the increased SH intensities, the hot spot regions in the stitched arrays seem to be spatially more confined compared the hot spots of the single array. In order to put this statement on a more stable ground, we have calculated spatial autocorrelation function $C_{s,x}(\Delta x)$ and $C_{s,y}(\Delta y)$ of the most dominant hot spots in each of the three sample along x and y, indicated by the black- and red-dotted crosses. These spatial autocorrelation traces are used to describe the spatial extend of speckle pattern and, hence, of weakly localized photonic [30, 31] or plasmonic modes [32, 33] in randomly arranged, scattering media. The spatial (second-order) autocorrelation function along the x-axis from $x_{\min}$ to $x_{\max}$ for a fixed position y = constant is defined as

$$C_s(\Delta x, y = \text{const.}) = \int_{x_{\min}}^{x_{\max}} (I_{SH,b}(x) \cdot I_{SH,b}(x + \Delta x))dx \Big/ \int_{x_{\min}}^{x_{\max}} (I_{\text{SH},b}(x)^2)dx \quad (2)$$

and equivalently along the y-axis. Here, $I_{\text{SH},b}(x,y) = I_{\text{SH}}(x,y) - \frac{1}{A}\iint I_{\text{SH}}(x,y)dxdy$ is the intensity at the SH, corrected by the spatially-averaged background around the hotspot that contains no relevant information [34]. The spatial autocorrelation traces along both axes are displayed in Figure 4(a) for the hot spot in the dimer structure, in (b) for the hot spot in the single array of the hexagonal patterns, and in (c) for the stitched array.

The FWHM of the autocorrelation function C_s – named correlation length l_c – can now be taken as a measure for the spatial extension of the localized plasmon modes. In other words, spatial correlation in the silver film is lost when moving the sample by more than one correlation length $l_{c,x}$ and $l_{c,y}$ along x and y, respectively [35].

As can be seen in Figure 4(a), this correlation length for the dimer structure is 880 nm along the x-direction, i.e., perpendicular to the dimer axis. Here, the measurement can be interpreted as a convolution between the spatial resolution of the SH microscope, indicated by the green solid line and the extent of the mode profile along the x-axis. Along the y-direction, i.e. parallel to the dimer axis, the autocorrelation length is 1050 nm, slightly larger than along the x-direction, due to the extension of the dimer structure in this direction.

For the single array of hexagonal patterns in (b), l_c increases significantly to 3.2 µm (FWHM) for the x-direction

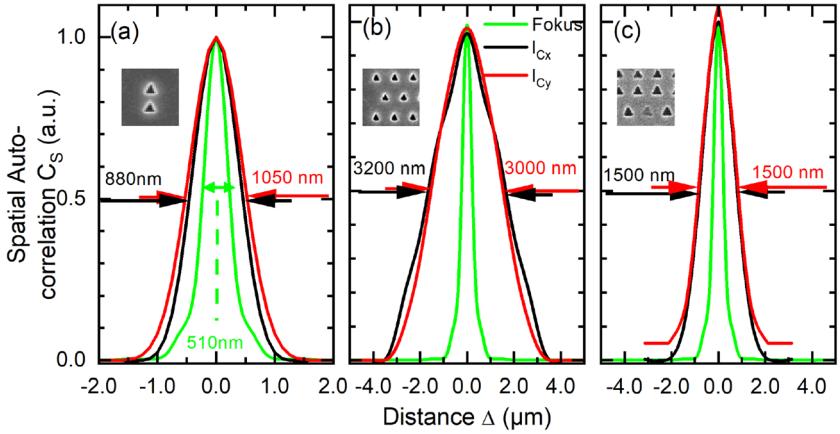

Figure 4: (a–c) Spatial autocorrelation trace $C_s(\Delta)$ along the x- (black) and the y-direction (red) for the most dominant hot spot of each sample, indicated by the black/red-dotted crosses in Figure 3. The green line represents the spatial resolution of the second harmonic (SH) microscope. For the dimer structure in (a), the spatial autocorrelation length $l_{c,x}$ along the x-axis is smaller than $l_{c,y}$, reflecting the extension of the triangular dimer structure along the y-axis. (b) + (c) The measured autocorrelation length increases to 3200 nm for the x-direction and to 3000 nm for the y-direction for the array of hexagonal pattern (b) and decreases again to 1500 nm for both the x- and y-axes for the stitched array in (c). The trace for the y-axis in (c) is slightly shifted for better visibility.

and 3.0 μm (FWHM) for the *y*-direction. Here, the modes tend to delocalize due to the coupling of neighboring triangles, almost independent for the *x*- and *y*-direction. In (c), the spatial autocorrelation trace for the most dominant hotspot of Sample 3 is displayed. The trace of C_s for the *y*-axis is shifted vertically for better visibility. For this sample, l_c decreases again by an about factor of 2–1.5 μm (FWHM) for both the *x*- and the *y*-direction. Here, l_c is only slightly larger than the diameter of the hexagonal unit cell $2 \cdot d_3$. The smaller correlation length for the stitched array can be well explained by the defects inside the hexagonal array that lead to a stronger localization compared to the single, unstitched array. Evidently, some fluctuations of the SH yield are also seen on the silver film that is surrounding the nanocavity arrays. These fluctuations reflect a finite degree of plasmon localization that results from multiple scattering of plasmon waves during their propagation along the interface. Since they are much weaker than the fluctuations seen within the array, they have little impact on the main findings discussed above.

Now, for a system of such spatially confined, enhanced electric fields, energy transfer from the localized modes to other modes in their close proximity via an exchange of propagating surface plasmon polaritons is hindered. The damping of the local electric fields, therefore, originates purely from radiative and nonradiative damping, as in the case of particle plasmons [36]. The damping time – or dephasing time – T_2 of the local electric field in one of these

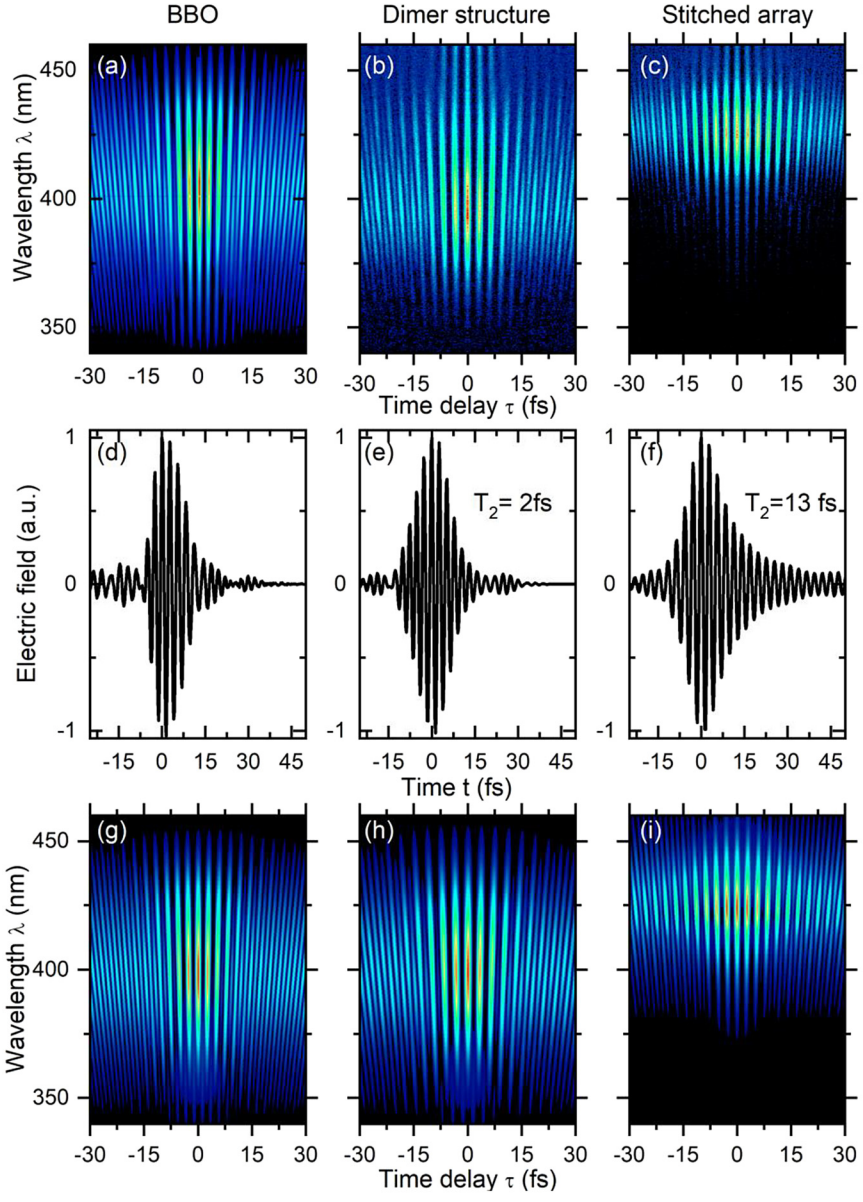

Figure 5: (a)–(c) Measured and reconstructed (g)–(i) IFRAC traces $I_F(\lambda, t)$ of a BBO crystal ((a) + (d)), the most dominant hot spot in the dimer structure ((b) + (h)) and in the stitched array ((c) + (i)). In addition to coherent SH emission (straight tilted lines), the traces in (b) and (c) show weak incoherent MPL (straight vertical lines) for wavelengths smaller than 450 nm. (d)–(f) Time structure of the local electric field reconstructed from the IFRAC trace of (d) the BBO crystal, (e) the dimer hot spot with lifetime of 2 fs, and (f) the stitched array hot spot with the lifetime of 13 fs.

strongly spatially localized hot spots should, therefore, be larger than for a spot in which the field can decay due to the emission of propagating SPP waves [37].

In contrast to incoherent microscopy techniques such as dark-field or photothermal microscopy, ultrafast SH microscopy can now give direct access to these lifetimes [2,38–40]. For this, however, a temporal resolution better than the few-femtosecond dephasing time of the electric fields is mandatory.

In order to map the damping of the local electric fields in the hot spots in the time domain, interferometric frequency-resolved autocorrelation (IFRAC) microscopy with a diffraction-limited spatial resolution can be employed. In the recent past, IFRAC and very familiar nonlinear interferometric techniques have been commonly used to determine the time structure of the electric field emitted from various nanostructures with femtosecond temporal resolution [22, 24, 41]. Generally, the IFRAC trace at a fixed position on the sample can be written as

$$I_F(\lambda,\tau) = \left| \int E_{\mathrm{NL}}(t,\tau)\cdot e^{-i2\pi c_0\cdot t/\lambda_C} dt \right|^2 \qquad (3)$$

with, E_{NL} as the electric SH field that is emitted from the sample after excitation with a phase-locked pulse pair $E(t)+E(t+\tau)$ at the fundamental wavelength λ_C. When assuming an instantaneous, spectrally-independent SH process, E_{NL} is simply given by $E_{\mathrm{SH}} \propto (E(t)+E(t+\tau))^2$and the corresponding local electric field at the fundamental can in principle be extracted using a commercial frequency-resolved optical gating (FROG) algorithm [42].

At first, the time structure of the incoming electric field was characterized by means of a 10 µm thick beta barium borate (BBO) crystal as a reference. The SH-IFRAC trace is displayed in Figure 5(a). The IFRAC trace consists of straight lines that are parallel along the wavelength axis for zero time delay and that start to tilt for negative and positive delays [25]. In the spectral domain, the SH emission covers a range between 340 and 460 nm with a maximum around 400 nm and a spectral width at full width of half maximum of $\Delta\lambda$ = 52 nm. The laser field $E_{\mathrm{BBO}}(t)$ that is inducing the SH emission in BBO is reconstructed using a commercial FROG algorithm. It is shown in (d) and its time structure is similar to that of the bandwidth-limited 6-fs incident pulse, centered at λ_C = 800 nm. Slight oscillations at negative time delays correspond most likely to the nonzero FROG error during the reconstruction.

To verify the results, the IFRAC trace for the BBO crystal $I_{F,\mathrm{BBO}}(\lambda,\tau)$ was simulated based on the reconstructed electric field $E_{\mathrm{BBO}}(t)$ at the fundamental wavelength. The result is depicted in Figure 5(g).

Here, no significant differences between the measured (a) and the simulated (g) IFRAC trace could be found, demonstrating the reliability of the reconstruction procedure for the electric field.

This reconstruction is now used to extract the electric field emitted from two hot spots with high SH intensity in the dimer structure in Sample 1 (Figure 5(b)) and in the stitched array in Sample 3 (Figure 5(c)). In the dimer array, the SH hot spot spectra are very similar to that emitted from the BBO crystal. The spectrum is centered around 400 nm and has a width of $\Delta\lambda$ = 50 nm. In the stitched array, the SH spectrum is much narrower ($\Delta\lambda$ = 25 nm), and is red-shifted toward 425 nm.

In the IFRAC traces, coherent SH emission appears in the form of characteristic interference fringes with wavelength-dependent fringe period. In contrast, the interferences fringes that are seen for incoherent MPL are independent of the emission wavelength and appear in the form of vertical straight lines in the IFRAC traces [25, 43]. MPL contributions are seen at wavelengths between 440 and 460 nm in Figure 5(b and c). Even though they are weak compared the coherent SH signal, they make the use of a direct pulse retrieval technique challenging. We, therefore, used a forward convolution technique to extract hot spot lifetimes. For this, we assume that the time structure of the incident laser field, $E_0(t)$, that is driving the SH emission matches the one that is reconstructed from the BBO measurements, $E_0(t) \propto E_{\mathrm{BBO}}(t)$. We describe the response of the hot spot mode to the incident field by a phenomenological linear response function

$$r_{\mathrm{HS}}(t) \propto \Theta(t)\exp(-i\omega_{\mathrm{HS}}t)\exp(-\gamma t).$$

Here, ω_{HS} is the resonance frequency of the hot spot and $\gamma = 1/T_2$ the dephasing rate of the hot spot mode. $\Theta(t)$ denotes the step function. The local field at the array surface that is inducing the SH emission is then given by the convolution

$$E_{\mathrm{HS}}(t,\tau) = \int E_0(t)\cdot r(t-\tau)d\tau. \qquad (4)$$

The induced nonlinear emission $E_{\mathrm{NL}}(t) \propto E_{\mathrm{HS}}(t)^2$ then enters Eq. (3) that is used for the simulation of the IFRAC traces.

This leaves two independent parameters, the resonance frequency ω_{HS} and the dephasing time T_2, to reconstruct the measured IFRAC traces. The reconstructions in Figure 5(h and i) show that this approach works reasonably well, even though it neglects possible resonant enhancements of the SH field in the sample. For the dimer hot spot, we find that the local field at the sample surface that is creating the

SH decays with a dephasing time of about T_2 = 2 fs, corresponding to an energy relaxation time $T_1 = T_2/2$ of only 1 fs. This agrees well with the linewidth of the linear transmission shown in Fig. S2(b) of the Supplementary material. Such short lifetimes have also been reported for similar types of isolated metal nanoparticles [44]. The exact value of the dephasing time should of course taken with some care since it is much shorter than the pulse duration of 6 fs. In the IFRAC simulations, we find reasonable agreement between experiment and simulation for resonance energy of $\hbar\omega_{HS}$ = 2.2 eV, i.e., the resonance energy of the linear transmission spectrum. Since the sample is off-resonantly excited, the results are of course not very sensitive to the exact value of ω_{HS} and similar experiment-theory match could be reached for other off-resonant excitation scenarios.

The results for the stitched array are fundamentally different. Here, the reconstructed field (Figure 3f) reveals quite clearly the free induction decay of a localized mode with a much longer dephasing time of T_2 = 13 fs. The resonance now is now red-shifted to 425 nm, in agreement with the SH spectrum shown in Figure 3. We recall that the linear spectra in Fig. S2 suggest that also in this case, the sample is excited at energies below the triangular hole resonance. We, therefore, suggest that both the distinct increase in lifetime and the spectral shift of the SH emission are distinct signatures of plasmon localization due to multiple scattering of SPP waves within the disordered triangle array. Together with the clear increase in spatial autocorrelation length of the SH emission when going from an individual dimer to a triangle array, this provides strong experimental evidence for the coupling of the triangles to SPP modes of the embedding silver film. The significant increase in local SH harmonic intensity in the stitched array and the decrease in correlation length upon stitching suggest that both local field enhancement and mode lifetime of the hot spot modes can be engineered by tailoring the long-range, micron-scale disorder in the array.

4 Conclusion

In summary, we have investigated experimentally the spatio-temporal trapping and hot-spot formation of SPP waves in different triangular nano-holes arrays of silver using ultrafast second harmonic microscopy. We have compared the SH local fluctuations of several structures, with the same triangular cavity sub-unit, and found that local dislocations and defects can increase the SH response up to factor of ~17 compared to a silver film.

A pronounced redshift of the SH spectrum for areas of high field localization within the hexagonal triangle array, as compared to that of individual triangle dimers, indicate that the SH is due to a far-field dark mode of the array. We attribute the enhanced fields within these hot spots to the coherent superposition of different randomly scattered surface plasmon polariton modes off-resonantly excited at the nanostructured silver film. Measurements of the hot spot diameters within the samples reveal that the most dominant hot spot is confined to 500–700 nm, approximately the inter-triangle distance d_3 of the hexagonal pattern. This conclusion is supported by IFRAC measurements of single hot spots in the dimer structure and the stitched array that are compared to IFRAC traces from a thin BBO crystal. From these measurements, the time structure of the electric field emitted from the hot spot is reconstructed. While the electric field from the hot spot in the dimer structure was very similar to the field from the incoming laser field and could be reproduced by a convolution of the incoming field with a field decay time of T_2 = 2 fs, the time structure significantly changed for the hot spot in the stitched array. Here, the best agreement between measured and reconstructed IFRAC trace was found for a local hot spot electric field with a decay time of T_2 = 13 fs.

Our results show a correlation between the spatial localization of plasmonic modes in a hot spot and the enhanced lifetime of the electric field emitted from the hot spot. They indicate both local field enhancement and mode lifetimes and, thus, nonlinear optical yield, can be engineered by jointly tailoring coherent couplings and mesoscopic disorder within plasmonic arrays. In the future, it will be interesting to further explore this degree of freedom by probing the spatio-temporal mode localization in specifically designed plasmonic nanostructures.

Author contributions: M.M. and S.S. built up the optical set-up, performed the experiments together with A.S., H.K., and M.S. The data were analyzed by A.S., H.K., and M.S. The samples were prepared by A.S. and M.M. C.L., A.S., and Y.P. initiated the experiment. The analytical modeling of the data was done by C.L. together with M.S. FDTD and IFRAC simulations were performed by M.S. The manuscript was written through contributions of all authors. All authors have given approval to the final version of the manuscript.

Research funding: Financial support by the Deutsche Forschungsgemeinschaft (SPP1839 and SPP1840, the Korea Foundation for International Cooperation of Science and Technology (Global Research Laboratory project, K20815000003), and the German-Isreali Foundation (Grant no. 203785), and the Graduate Program Nanoenergy of the State of Lower Saxony is

gratefully acknowledged. M. S. wishes to thank the BMBF for a personal research grant "Photonic transistors" in the NanoMatFutur program.

Conflict of interest statement: The authors declare no conflicts of interest regarding this article.

References

[1] T. Klar, M. Perner, S. Grosse, G. von Plessen, W. Spirkl, and J. Feldmann, "Surface-plasmon resonances in single metallic nanoparticles," *Phys. Rev. Lett.*, vol. 80, pp. 4249–4252, 1998.

[2] T. V. Shahbazyan and M. I. Stockman, *Plasmonics: Theory and Applications*, Springer, 2013.

[3] D. S. Kim, S. C. Hohng, V. Malyarchuk, et al., "Microscopic origin of surface-plasmon radiation in plasmonic band-gap nanostructures," *Phys. Rev. Lett.*, vol. 91, p. 143901, 2003.

[4] A. Salomon, Y. Prior, M. Fedoruk, J. Feldmann, R. Kolkowski, and J. Zyss, "Plasmonic coupling between metallic nanocavities," *J. Opt.*, vol. 16, p. 114012, 2014.

[5] T. Maurer, P.-M. Adam, and G. Lévêque, "Coupling between plasmonic films and nanostructures: from basics to applications," *Nanophotonics*, vol. 4, pp. 363–382, 2015.

[6] A. Weissman, M. Galanty, D. Gachet, E. Segal, O. Shavit, and A. Salomon, "Spatial confinement of light onto a flat metallic surface using hybridization between two cavities," *Adv. Opt. Mater.*, vol. 5, p. 1700097, 2017.

[7] S. Grésillon, L. Aigouy, A. C. Boccara, et al., "Experimental observation of localized optical excitations in random metal-dielectric films," *Phys. Rev. Lett.*, vol. 82, pp. 4520–4523, 1999.

[8] D. A. Genov, A. K. Sarychev, V. M. Shalaev, and A. Wei, "Resonant field enhancements from metal nanoparticle arrays," *Nano Lett.*, vol. 4, pp. 153–158, 2004.

[9] M. I. Stockman, D. J. Bergman, C. Anceau, S. Brasselet, and J. Zyss, "Enhanced second-harmonic generation by metal surfaces with nanoscale roughness: nanoscale dephasing, depolarization, and correlations," *Phys. Rev. Lett.*, vol. 92, p. 057402, 2004.

[10] S. I. Bozhevolnyi, B. Vohnsen, I. I. Smolyaninov, and A. V. Zayats, "Direct observation of surface polariton localization caused by surface roughness," *Opt. Commun.*, vol. 117, pp. 417–423, 1995.

[11] B. Dragnea, J. M. Szarko, S. Kowarik, T. Weimann, J. Feldmann, and S. R. Leone, "Near-field surface plasmon excitation on structured gold films," *Nano Lett.*, vol. 3, pp. 3–7, 2003.

[12] S. I. Bozhevolnyi and V. Coello, "Statistics of local field intensity enhancements at nanostructured surfaces investigated with a near-field optical microscope," *Phys. Rev. B*, vol. 64, p. 115414, 2001.

[13] M. Galanty, O. Shavit, A. Weissman, et al., "Second harmonic generation hotspot on a centrosymmetric smooth silver surface," *Light Sci. Appl.*, vol. 7, p. 49, 2018.

[14] X. Xue, Y. Fan, E. Segal, et al., "Periodical concentration of surface plasmon polaritons by wave interference in metallic film with nanocavity array," *Mater. Today*, 2021. https://doi.org/10.1016/j.mattod.2020.12.016, in press.

[15] P. Kahl, D. Podbiel, C. Schneider, et al., "Direct observation of surface plasmon polariton propagation and interference by time-resolved imaging in normal-incidence two photon photoemission microscopy," *Plasmonics*, vol. 13, pp. 239–246, 2017.

[16] C. Lemke, C. Schneider, T. Leißner, et al., "Spatiotemporal characterization of SPP pulse propagation in two-dimensional plasmonic focusing devices," *Nano Lett.*, vol. 13, pp. 1053–1058, 2013.

[17] E. Segal, M. Galanty, H. Aharon, and A. Salomon, "Visualization of plasmon-induced hot electrons by scanning electron microscopy," *J. Phys. Chem. C*, vol. 123, pp. 30528–30535, 2019.

[18] M. Breit, V. A. Podolskiy, S. Grésillon, et al., "Experimental observation of percolation-enhanced nonlinear light scattering from semicontinuous metal films," *Phys. Rev. B*, vol. 64, p. 125106, 2001.

[19] V. M. Shalaev and A. K. Sarychev, "Nonlinear optics of random metal-dielectric films," *Phys. Rev. B*, vol. 57, pp. 13265–13288, 1998.

[20] H. Aharon, O. Shavit, M. Galanty, and A. Salomon, "Second harmonic generation for moisture monitoring in dimethoxyethane at a gold-solvent interface using plasmonic structures," *Nanomaterials*, vol. 9, p. 1788, 2019.

[21] B. Piglosiewicz, D. Sadiq, M. Mascheck, et al., "Ultrasmall bullets of light-focusing few-cycle light pulses to the diffraction limit," *Opt. Express*, vol. 19, pp. 14451–14463, 2011.

[22] G. Stibenz and G. N. Steinmeyer, "Interferometric frequency-resolved optical gating," *Opt. Express*, vol. 13, pp. 2617–2626, 2005.

[23] J. Hyyti, E. Escoto, and G. Steinmeyer, "Third-harmonic interferometric frequency-resolved optical gating," *J. Opt. Soc. Am. B*, vol. 34, pp. 2367–2375, 2017.

[24] M. Mascheck, S. Schmidt, M. Silies, et al., "Observing the localization of light in space and time by ultrafast second-harmonic microscopy," *Nat. Photonics*, vol. 6, pp. 293–298, 2012.

[25] S. Schmidt, M. Mascheck, M. Silies, et al., "Distinguishing between ultrafast optical harmonic generation and multi-photon-induced luminescence from ZnO thin films by frequency-resolved interferometric autocorrelation microscopy," *Opt. Express*, vol. 18, pp. 25016–25028, 2010.

[26] A. Salomon, M. Zielinski, R. Kolkowski, J. Zyss, and Y. Prior, "Size and shape resonances in second harmonic generation from silver nanocavities," *J. Phys. Chem. C*, vol. 117, pp. 22377–22382, 2013.

[27] N. J. Halas, S. Lal, W.-S. Chang, S. Link, and P. Nordlander, "Plasmons in strongly coupled metallic nanostructures," *Chem. Rev.*, vol. 111, pp. 3913–3961, 2011.

[28] J.-M. Yi, D. Hou, H. Kollmann, et al., "Probing coherent surface plasmon polariton propagation using ultrabroadband spectral interferometry," *ACS Photonics*, vol. 4, pp. 347–354, 2017.

[29] J. E. Kihm, Y. C. Yoon, D. J. Park, et al., "Fabry-Perot tuning of the band-gap polarity in plasmonic crystals," *Phys. Rev. B*, vol. 75, p. 035414, 2007.

[30] P. Sebbah, B. Hu, A. Z. Genack, R. Pnini, and B. Shapiro, "Spatial-field correlation: the building block of mesoscopic fluctuations," *Phys. Rev. Lett.*, vol. 88, p. 123901, 2002.

[31] V. Emiliani, F. Intonti, M. Cazayous, et al., "Near-field short range correlation in optical waves transmitted through random media," *Phys. Rev. Lett.*, vol. 90, p. 250801, 2003.

[32] J. Laverdant, S. Buil, B. Bérini, and X. Quélin, "Polarization dependent near-field speckle of random gold films," *Phys. Rev. B*, vol. 77, p. 165406, 2008.
[33] J. Laverdant, S. Buil, J.-P. Hermier, and X. Quelin, "Near-field intensity correlations on nanoscaled random silver/dielectric films," *J. Nanophotonics*, vol. 4, p. 049505, 2010.
[34] U. Neuberth, L. Walter, G. von Freymann, et al., "Spatial autocorrelation analysis of nanophotoluminescence images of single GaAs quantum wells," *Appl. Phys. Lett.*, vol. 81, pp. 1881–1883, 2002.
[35] A. P. Mosk, A. Lagendijk, G. Lerosey, and M. Fink, "Controlling waves in space and time for imaging and focusing in complex media," *Nat. Photonics*, vol. 6, pp. 283–292, 2012.
[36] M. I. Stockman, "Femtosecond optical responses of disordered clusters, composites, and rough surfaces: "The Ninth Wave" effect," *Phys. Rev. Lett.*, vol. 84, pp. 1011–1014, 2000.
[37] J. Bosbach, C. Hendrich, F. Stietz, T. Vartanyan, and F. Träger, "Ultrafast dephasing of surface plasmon excitation in silver nanoparticles: influence of particle size, shape, and chemical surrounding," *Phys. Rev. Lett.*, vol. 89, p. 257404, 2002.
[38] A. Anderson, K. S. Deryckx, X. G. Xu, G. Steinmeyer, and M. B. Raschke, "Few-femtosecond plasmon dephasing of a single metallic nanostructure from optical response function reconstruction by interferometric frequency resolved optical gating," *Nano Lett.*, vol. 10, pp. 2519–2524, 2010.
[39] T. Hanke, J. Cesar, V. Knittel, et al., "Tailoring spatiotemporal light confinement in single plasmonic nanoantennas," *Nano Lett.*, vol. 12, pp. 992–996, 2012.
[40] S. Schmidt, B. Piglosiewicz, D. Sadiq, et al., "Adiabatic nanofocusing on ultrasmooth single-crystalline gold tapers creates a 10-nm-sized light source with few-cycle time resolution," *ACS Nano*, vol. 6, pp. 6040–6048, 2012.
[41] S. Berweger, J. M. Atkin, X. G. Xu, R. L. Olmon, and M. B. Raschke, "Femtosecond nanofocusing with full optical waveform control," *Nano Lett.*, vol. 11, pp. 4309–4313, 2011.
[42] L. Xu, E. Zeek, and R. Trebino, "Simulations of frequency-resolved optical gating for measuring very complex pulses," *J. Opt. Soc. Am. B*, vol. 25, pp. A70–A80, 2008.
[43] C. K. Chen, A. R. B. de Castro, and Y. R. Shen, "Surface-enhanced second-harmonic generation," *Phys. Rev. Lett.*, vol. 46, pp. 145–148, 1981.
[44] T. Hanke, G. Krauss, D. Trautlein, B. Wild, R. Bratschitsch, and A. Leitenstorfer, "Efficient nonlinear light emission of single gold optical antennas driven by few-cycle near-infrared pulses," *Phys. Rev. Lett.*, vol. 103, p. 257404, 2009.

Supplementary Material: The online version of this article offers supplementary material (https://doi.org/10.1515/nanoph-2021-0049).